Insights of Electrical Engineering and Technology
https://www.achpub.com/IEET
Communication

Highly Isolated Dual Circularly Polarized Metallic ME-dipole Antenna Array Design

Oludayo Sokunbi*, Ahmed A. Kishk

Department of Electrical and Computer Engineering, Concordia University, Montreal, QC H3G 1M8, Canada
* Correspondence: sokunbidayo@gmail.com

Received: 17 June 2025 **Revised:** 10 July 2025 **Accepted:** 21 July 2025 **Published:** 21 August 2025

Abstract: A novel dual circularly polarized metallic magneto-electric dipole (D-CP-M-ME-dipole) for the 30 GHz band is presented. The element is made of solid aluminum and has no surrounding metallic cavity. It is fed through crossed narrow slots coupled to air-filled microstrip lines with a bed of periodic printed mushroom structures, achieving a bandwidth of 26–41 GHz (46%). An 8×8 array uses a dual-polarized corporate feed network optimized to account for mutual coupling. This design eliminates the need for an external mechanism to decouple the two polarizations. The feed network is implemented in printed gap waveguide (PGW) technology to suppress leakage. Adding parasitic elements to the 8×8 array yields a 9×9 array and improves gain across the operating band. Measurements of the fabricated 9×9 dual circularly polarized metallic magnetoelectric dipole array show an impedance bandwidth of 26–42 GHz (47%), a gain of 26.6 dBic, and a total efficiency of 90%. The isolation between the two polarizations is less than 40 dB across the band.

Keywords: magnetoelectric dipole; microstrip ridge gap waveguide (MRGW); circular polarization; antenna arrays

1. Introduction

Dual circularly polarized antennas can reduce polarization mismatch, mitigate multipath effects, support mobile operation, and reduce interference. They produce two orthogonal electric-field components of equal amplitude in phase quadrature ($\pm 90^\circ$), yielding right-hand circular polarization (RHCP) or left-hand circular polarization (LHCP) [1]. These properties make them suitable for satellite navigation, aerospace, radar, and mobile communications [2]. The 3-dB axial-ratio (AR) bandwidth of circularly polarized (CP) antennas typically exceeds 15%. Most CP arrays use a sequential-rotation feed network to meet this bandwidth requirement. CP antenna feeds can be classified as single-probe or multiprobe, depending on the bandwidth requirement.

A 4-layer dual circularly polarized 8×8 array for the K band used two stacked chamfered square patches and two orthogonal slots [3]. It achieved dual circular polarization over 18.8–20 GHz, with polarization isolation below 15 dB and an aperture efficiency of 75%. A single-layer antenna with a sequential-rotation feed network achieved dual circular polarization over 27–33 GHz, with isolation below 20 dB and a gain of 11.8 dBi [4]. Two suspended metal posts and two semicircular patches with orthogonal slots were used to achieve dual circular polarization in a 4-layer 4×4 patch antenna over 26–35 GHz, with a peak gain of 14.5 dBi [5]. The 3-layer 2×2 array [6] used a printed ridge gap waveguide (PRGWG) and stacked patches to generate LHCP in the 20 GHz band and RHCP in the 30 GHz band. The array achieved AR bands of 19.4–20.4 GHz and 28.5–31.4 GHz, with gains of 13.2 and 11.5 dBic, respectively. Dynamic and Berry phase compensation were used in a low-profile 2×2 dual-CP antenna with a peak gain of 28 dBic and an AR band of 27–36 GHz [7]. A 4-layer 2×2 array employing 90° sequential rotation and a feed network achieved a 3-dB AR and impedance bandwidth of 57–72.3 GHz (23.8%), with a peak gain of 20.5 dBic [8].

A dual-band CP antenna reused the feed network of a magnetoelectric dipole (ME-dipole) as a radiating slot antenna [9]. The patches generated LHCP, and the microstrip line and slot generated RHCP. A polarization converter [10] converted radiation from a four-port linearly polarized (LP) multiple-input multiple-output (MIMO) antenna to CP over the upper and lower bands of 29.25–30.35 GHz and 19.65–22.05 GHz, respectively. A polarization-twisting metasurface converted LP to dual circular polarization over the Ku-band ranges of 12.25–12.95 GHz and 14.00–14.55 GHz [11]. The metasurface consisted of a dual-linear-to-circular polarization converter (DLCPC) and a linear polarization conversion metasurface (LPCM). A partially reflective surface (PRS) was added to a dual LP feed network to produce dual circular polarization [12]. A partially reflecting metasurface was integrated into a Fabry–Pérot (FP) antenna to separate LP waves into RHCP

Copyright: ©2025 by the authors.
https://doi.org/10.64897/ieet.2025v1i1.001
This article is an open access article distributed under the terms and conditions of the Creative Commons Attribution (CC BY) license

and LHCP [13]. Varactor diodes tuned the operating band of a patch antenna, and a feed network loaded with PIN diodes converted LP to LHCP and RHCP [14]. The antenna could be tuned continuously from 2 to 2.7 GHz for both polarizations. A dual-polarized filtering antenna illuminated a dielectric lens. A CP polarizer and phase shifters enabled conversion from LP to dual circular polarization around 60 GHz [15]. Other designs achieved filtering by cascading a bandpass filter with a CP antenna [16,17] or by coupling a CP radiator to resonators [18,19]. A filtering power divider network can also excite two orthogonal modes to produce CP [20–25].

Wide millimeter-wave (mm-wave) bands support high capacity and high data rates. Atmospheric attenuation can limit long-range mm-wave links, so high-gain antennas are often used to compensate for propagation losses [26]. Guiding structures in high-gain mm-wave antennas must be designed to minimize spurious radiation [27–32]. Substrate-integrated waveguides (SIWs) [33] and gap waveguides [34] are among the guiding structures used in mm-wave antennas.

This work presents an 8×8 array of dual circularly polarized metallic magnetoelectric dipoles (D-CP-M-ME-dipoles) fed by a microstrip printed gap waveguide. Each antenna element consists of 4 metallic pins and a crossed slot. A diagonal metallic strip placed between opposite corners of the pin structure perturbs the fields excited by the crossed slots. This produces two orthogonal linearly polarized modes with a relative phase shift of 90°, enabling LHCP and RHCP. Here, the ME-dipole element itself generates the two circular polarizations. Designs reported elsewhere generate them in multiple layers or in the feed network. The 3-dB axial-ratio and −10 dB impedance bands overlap over 26–42 GHz (47%). The corporate feed network is designed by extrapolating the mutual admittance matrix of the large 8×8 array from that of a smaller 4×4 array. The frequency-dependent effective impedance of the large array is then extracted from the smaller array, accounting for mutual coupling.

The proposed single-layer feed network adapts the design [35] for dual circular polarization. It uses frequency-dependent effective impedance terminations. Other reported dual-polarized feed networks use multiple layers to produce the polarizations. The proposed air-filled ME-dipole eliminates dielectric material to reduce dielectric losses and improve antenna efficiency. It achieves a wide impedance bandwidth with a cavity-free structure. The air-filled ME-dipoles in [36–39] use surrounding cavities. The main contributions are as follows:

1. Extending the array architecture for a single linear polarization [35] to support dual circular polarization, with frequency-dependent behavior that improves broadband performance.

2. Developing a compact, air-filled, dual-polarized ME-dipole with a cavity-free structure. Previous designs used a surrounding open cavity wall [36–39]. The proposed design reduces structural complexity while achieving a bandwidth of 46% and high radiation efficiency.

3. Improving the aperture power distribution in arrays larger than 4×4. In such arrays, single-layer feed networks increase the spacing between adjacent 4×4 subarrays relative to the spacing between individual elements, reducing gain and efficiency. Parasitic elements placed in the inter-subarray gaps are excited by the surrounding active elements. The resulting in-phase reradiation restores aperture continuity and improves overall gain and efficiency.

2. Design Mechanism

2.1. Unit Cell Design

First, the periodic structure is designed to provide a stop band with a lower-to-upper frequency ratio of approximately 1:2 [40]. The printed structure consists of periodic mushroom cells with a square cross section of $L_2 \times L_2$, as shown in Figure 1. Each cell has an $L_1 \times L_1$ square patch connected to the ground plane by a metallic via that is 0.3 mm in diameter and 0.508 mm long. The patch and the ground plane are on opposite sides of a Rogers RT 6002 substrate with a relative permittivity of 2.94 and a loss tangent of 0.0012. The microstrip line is printed on a 0.254 mm-thick RT 5880 substrate above the square patch. This substrate has a relative permittivity of 2.2 and a loss tangent of 0.0009. A 0.27 mm air gap separates the upper substrate from the upper conductor. The equivalent thickness of the air gap and the upper substrate must be much less than a quarter wavelength at the upper frequency. The resulting stop band extends from 25 to 50 GHz and suppresses wave propagation between the mushroom surface and the upper conductor. The microstrip line is then inserted to guide the signal between the line and the upper conductor, confining propagation to the direction of the line. These results are omitted for brevity.

https://doi.org/10.64897/ieet.2025v1i1.001

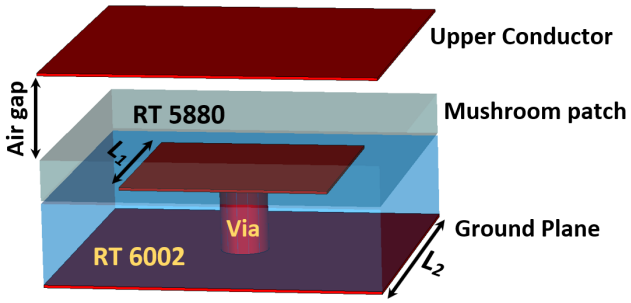

Figure 1. Mushroom unit cell ($L_1 = 0.79$ mm, $L_2 = 1$ mm).

2.2. Dual Circularly Polarized Metallic ME Dipole

The linearly polarized ME dipole [41], which is coupled to the feed lines through a slot, is modified to produce a dual circularly polarized metallic magnetoelectric dipole (D-CP-M-ME-dipole). A metallic strip spans two diagonally opposite pins and perturbs the fields excited by the crossed slots. This produces two orthogonal linearly polarized modes of equal amplitude with a 90° phase difference, enabling left- and right-hand circular polarization (LHCP and RHCP, respectively). The dipole requires 17 × 17 mushroom cells. Two orthogonal stubs, one etched at the tip of each feed line, minimize coupling and improve impedance matching. The two feed lines thus excite distinct polarizations through the air gap. Each feed line is 9 mm long and 0.7 mm wide and is positioned near the end of its corresponding slot. Each slot measures 0.5 mm × 6 mm. The dipole sits directly on the metallic plate, as shown in Figure 2(a). It consists of four metallic pins, each measuring 2 mm × 2 mm × 1.5 mm, and a 2.1 mm × 0.42 mm diagonal strip.

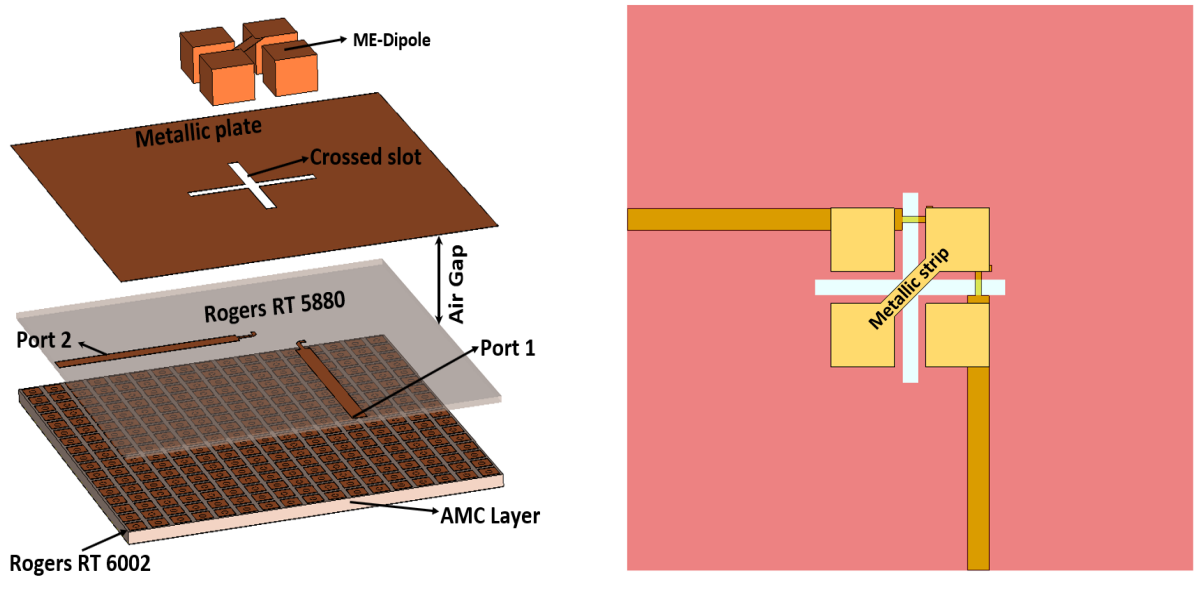

Figure 2. Dual circularly polarized metallic ME dipole. (a) Three-dimensional schematic. (b) Top view with the conductor sheet shown as transparent to reveal the feed lines.

Figure 2(b) shows the positions of the orthogonal feed lines relative to the crossed slots. The feed lines are approximately 0.5 mm from the slot edges. The top view also shows the metallic pins and the diagonal strip that produces circular polarization. Integrating the polarization conversion into the antenna simplifies the design. The feed lines excite distinct modes on the same layer, allowing a compact and flexible layout. The antenna measures 17.6 mm × 17.6 mm.

From 25 to 41 GHz, the single-element antenna meets the −10 dB impedance-matching criterion and exhibits an axial ratio below 3 dB and port isolation greater than 40 dB, as shown in Figure 3(a,b). The high isolation is achieved by the open-circuit stubs at the tips of the feed lines. The antenna has a peak gain of 11.7 dBic for both polarizations, as shown in Figure 4.

https://doi.org/10.64897/ieet.2025v1i1.001

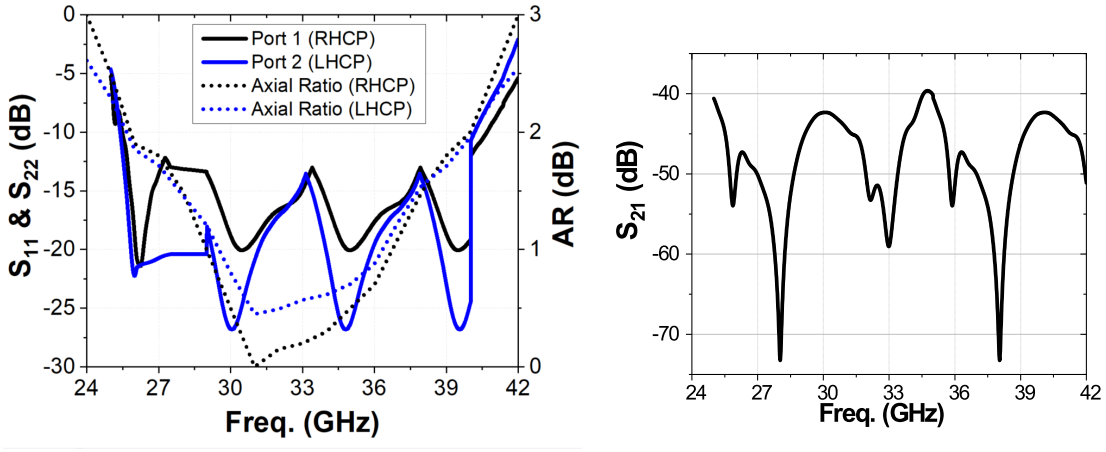

(a) **(b)**

Figure 3. (a) Reflection coefficients and axial ratios for RHCP and LHCP. (b) Transmission coefficient S_{21}, indicating port isolation greater than 40 dB.

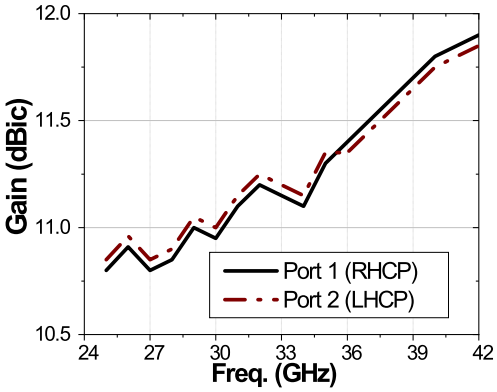

Figure 4. Gain of the dual circularly polarized metallic ME dipole element.

Figure 5 shows the far-field radiation patterns of the single element in the *xz* and *yz* planes at 28, 32, and 38 GHz. The cross-polarized patterns are omitted because the cross-polarization level is reported to be below 40 dBic at these frequencies.

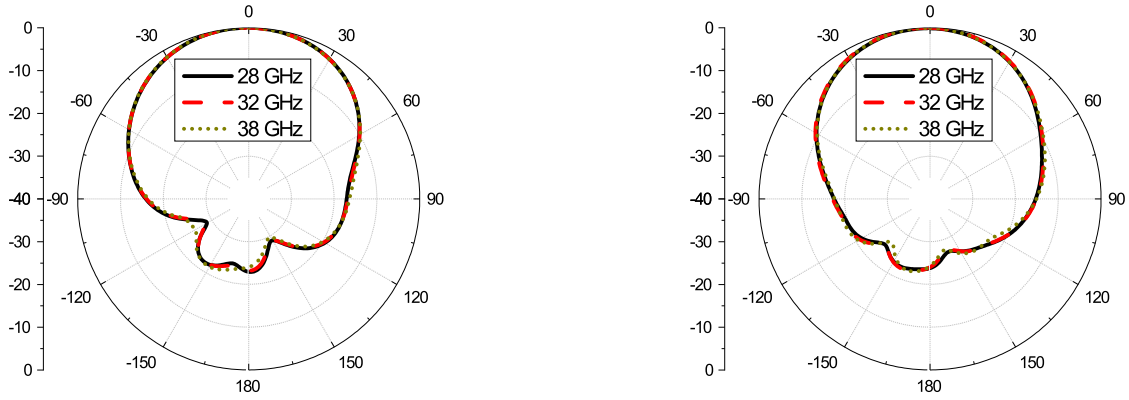

(a) **(b)**

Figure 5. Single-element far-field patterns for RHCP (a,b) and LHCP (c,d) in the *yz* (left) and *xz* (right) planes.

https://doi.org/10.64897/ieet.2025v1i1.001

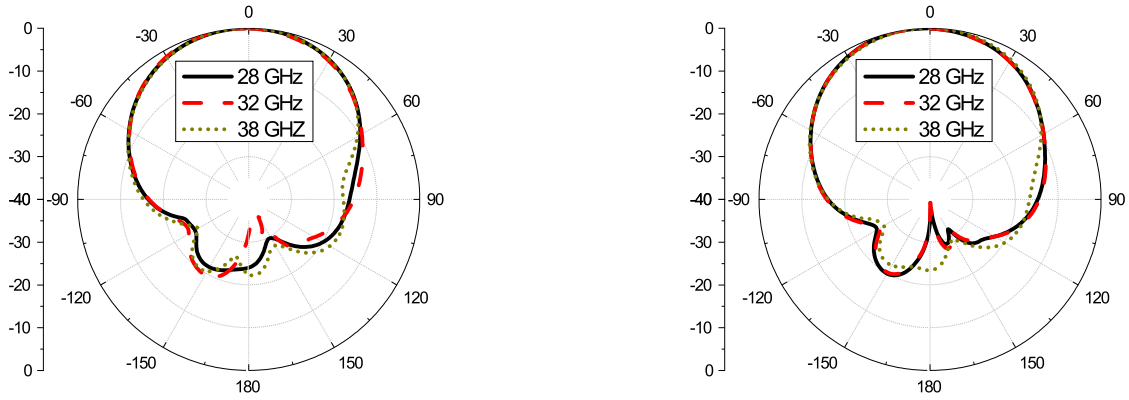

(c) **(d)**

Figure 5. Cont.

2.3. 8 × 8 CP Array Design

To design the 8 × 8 array, a 4 × 4 ME-dipole subarray is first designed without a feed network to extract the admittance matrix and the frequency-dependent input impedance of each element. The proposed single-layer feed network serves both polarizations, so the feed lines must not overlap or cross. The element spacings along the two axes are d_x and d_y. Figure 6 shows the 8 × 8 element arrangement. The separations between the edge elements of adjacent 4 × 4 subarrays are D_x and D_y. Figure 7 shows the resulting feed network.

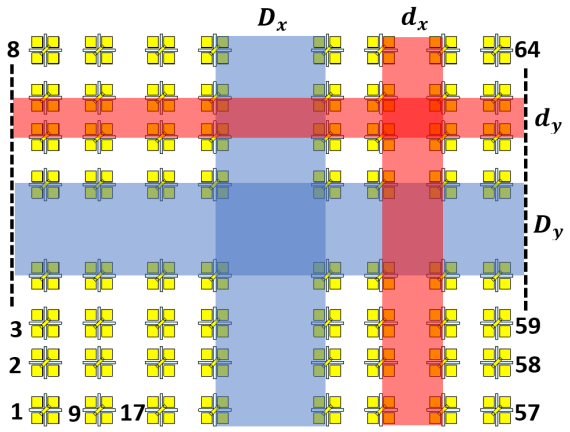

Figure 6. Element arrangement and numbering for the 8 × 8 array ($d_x = d_y = 0.83$ mm and $D_x = D_y = 1.54$ mm).

Parasitic elements are added to the gaps in the active 8 × 8 array (Figure 6), as shown in Figure 8. The parasitic elements are coupled to the active elements and act as secondary sources. They improve the power distribution across the array and thereby increase its gain. The parasitic elements are loaded with slots similar to those in the active elements. Figure 9 shows the fabricated array.

Figure 10 shows the simulated and measured reflection coefficients of the 9 × 9 array for RHCP and LHCP. Full-wave simulations include the entire structure and its radiating elements. In the effective-impedance termination model (Eff. Imp. ter. in the legend), frequency-dependent effective impedance loads replace the radiating elements at the feed-network ports.

Figure 11 shows the simulated and measured axial ratios for both polarizations. The axial-ratio bandwidth is 24–42 GHz (56%), which covers the anticipated impedance bandwidth.

Figure 12 shows the simulated and measured polarization isolation for configurations with radiating elements or impedance terminations. The reported isolation is less than 40 dB throughout the band. The high isolation is attributed to the feed network, which accounts for mutual coupling between the antenna elements and ports.

https://doi.org/10.64897/ieet.2025v1i1.001

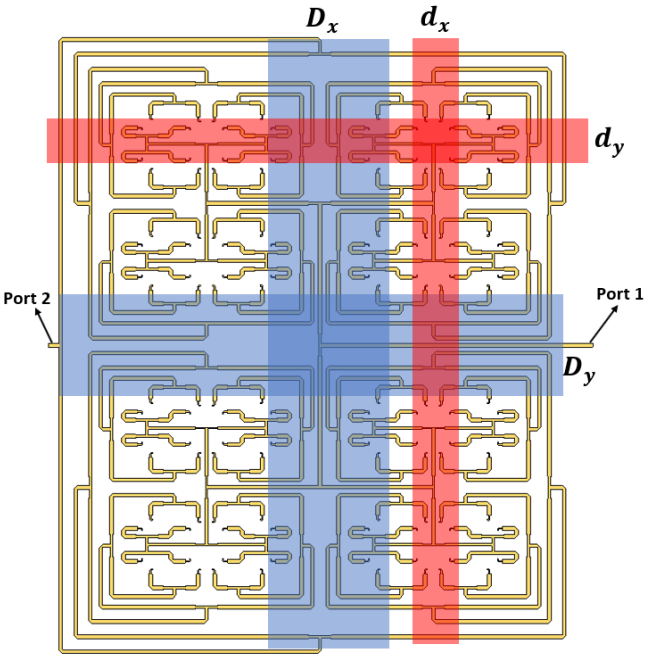

Figure 7. Constructed feed network for the 8 × 8 array.

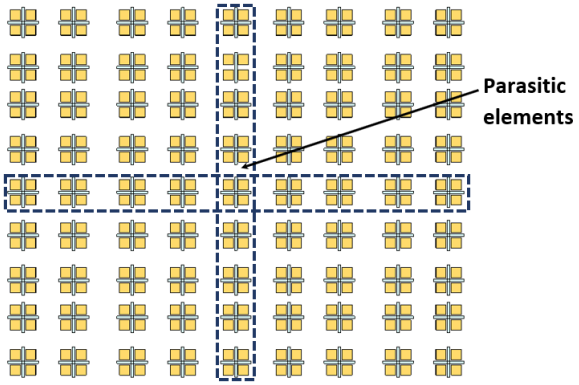

Figure 8. Feed network design for the 8 × 8 array with active and parasitic elements.

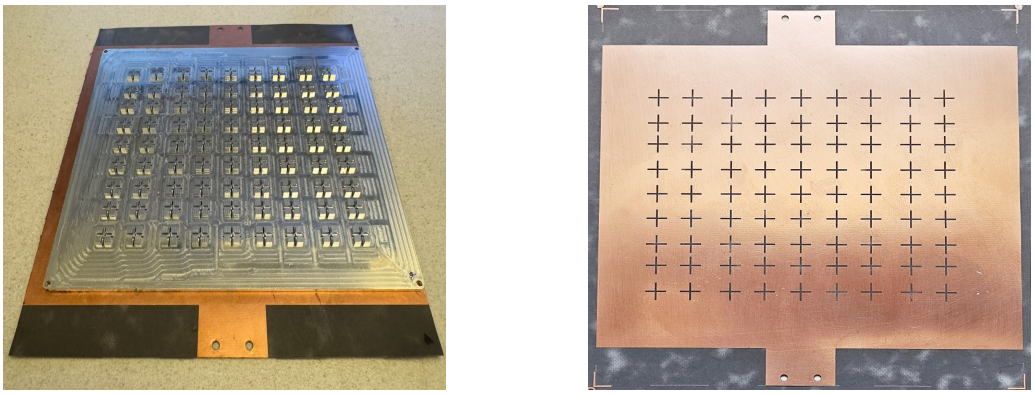

(a) **(b)**

Figure 9. Fabricated prototype of the 9 × 9 array: (a) top layer, (b) slot layer, (c) feed network, and (d) AMC layer.

https://doi.org/10.64897/ieet.2025v1i1.001

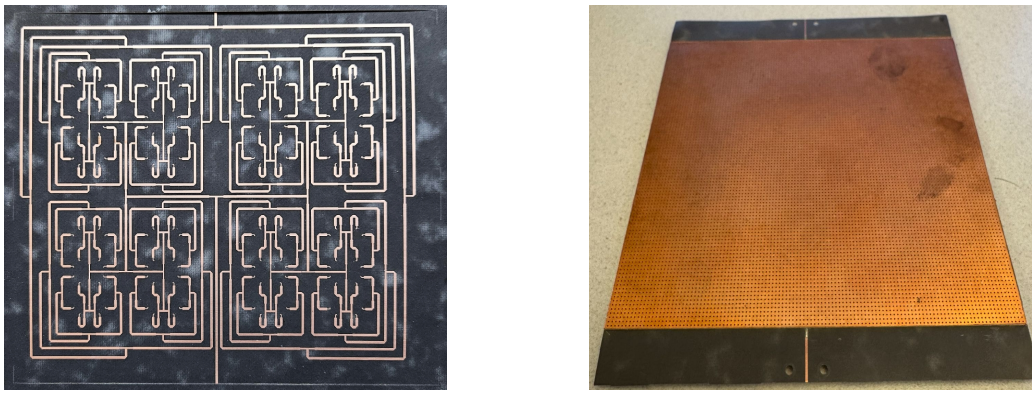

(c) **(d)**

Figure 9. Cont.

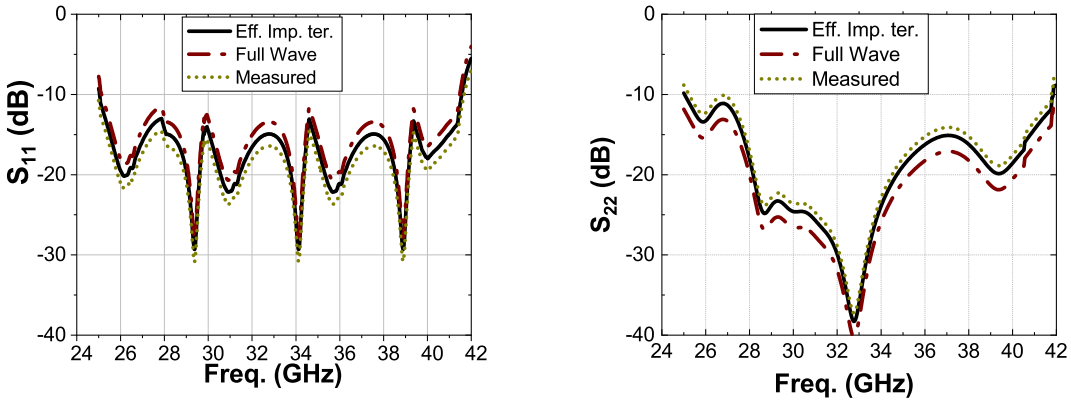

(a) **(b)**

Figure 10. Measured and simulated reflection coefficients of the 9 × 9 dual-CP metallic ME-dipole array: (a) RHCP and (b) LHCP.

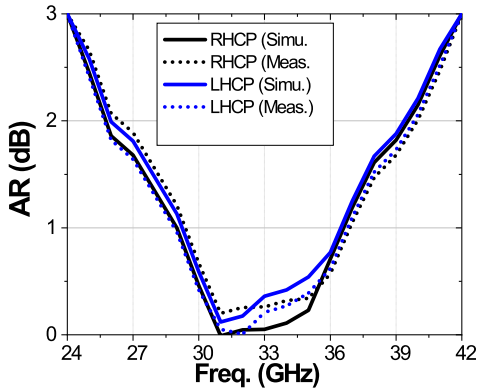

Figure 11. Simulated and measured axial ratios of the 9 × 9 dual-CP metallic ME-dipole array.

https://doi.org/10.64897/ieet.2025v1i1.001

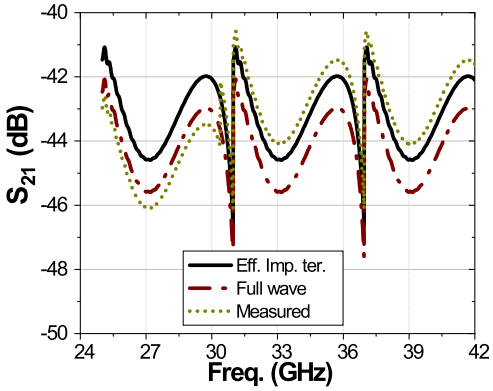

Figure 12. Simulated and measured isolation between the RHCP and LHCP ports of the 9 × 9 array.

The array gain is simulated with and without the parasitic elements. The measured gain of the array with the parasitic elements is compared with the simulated gain. The parasitic elements increase the array gain by an average of 0.2 dB and do not affect the *S*-parameters or the radiation pattern. Figure 13 also shows the corresponding simulated and measured total efficiencies. The antenna achieves a maximum efficiency of 89%.

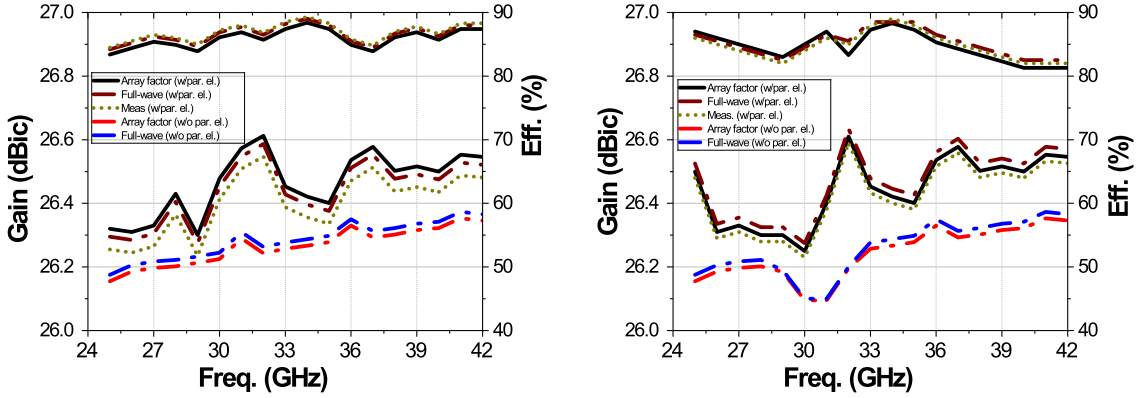

Figure 13. Simulated and measured gain and efficiency of the array: (a) RHCP and (b) LHCP.

Figure 14 shows the simulated and measured far-field radiation patterns of the 9 × 9 array at 34 GHz and compares the array-factor method with the full-wave simulation. The cross-polarized response is below 40 dB and is omitted from the plots. The patterns in the *xz* and *yz* planes are similar.

PGW can introduce losses in large antenna arrays that use a mushroom AMC. Mechanical tolerances can also be critical at millimeter-wave frequencies and could be investigated further using empirical equations. The approach of extrapolating from a small array to a large one can be extended to arbitrarily distributed arrays. Machine learning could be used to derive a model of a small, irregularly distributed array and use it to design a larger one. The attainable scanning range could also be evaluated.

Table 1 compares the proposed array with recently reported dual-polarized CP arrays. Among the designs listed, the proposed array offers the highest isolation, the widest bandwidth, and the highest peak gain, using two layers.

https://doi.org/10.64897/ieet.2025v1i1.001

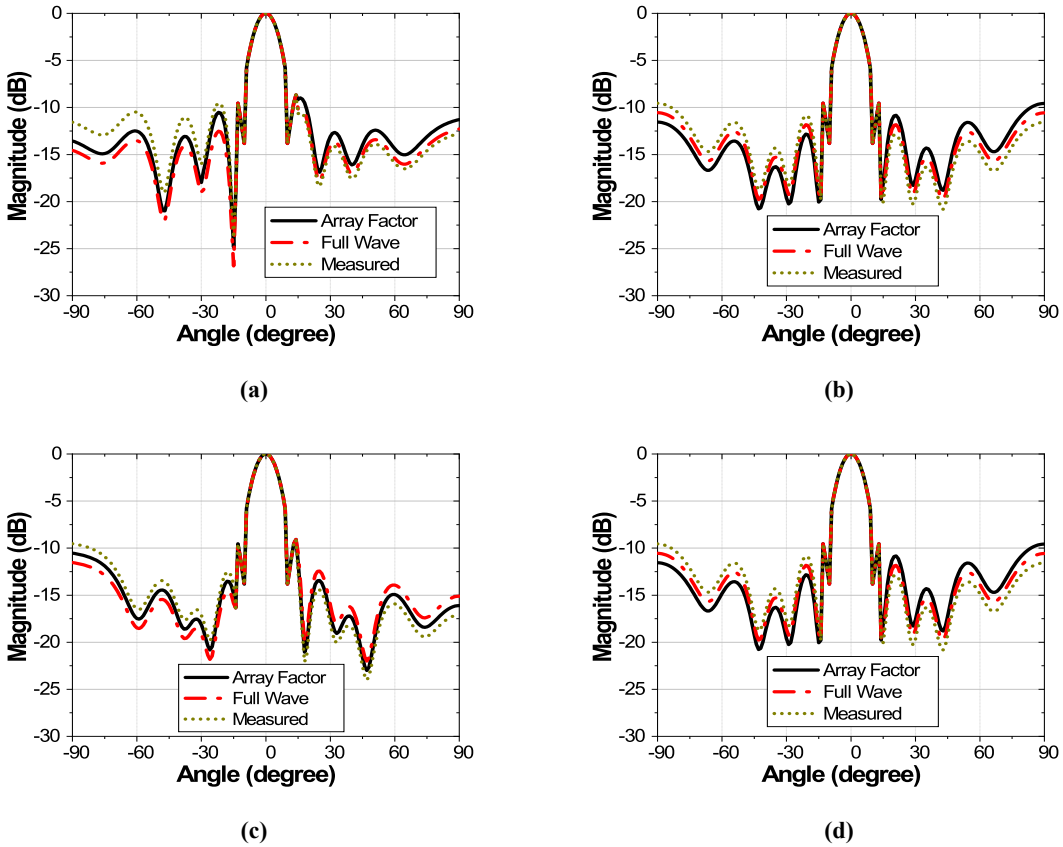

Figure 14. Normalized radiation patterns of the array at 34 GHz. The top and bottom rows show RHCP and LHCP, respectively. The right and left columns show the *xz* and *yz* planes, respectively.

Table 1. Comparison with other dual-polarized CP arrays reported in the literature.

Ref.	No. of Elements	Isolation (dB)	No. of Pol.	BW (%)	No. of Layers	Peak Gain (dBic)	Efficiency (%)
[42]	8×8	14	Dual-CP	23/23	6	25.8/25.7	80/80
[43]	4×4	15	Dual-CP	17/17	5	20.8/21.0	90/95
[44]	16×16	13	Dual-CP	16/16	8	32.8/32.8	90/90
Prop.	8×8	40	Dual-CP	47/47	2	26.61/26.62	89/90

3. Conclusions

A dual-circularly polarized metallic magnetoelectric dipole antenna with high isolation is presented. A diagonal metal strip converts the two linear polarizations to two circular polarizations. The design uses no dielectric substrate, which improves efficiency compared with other ME-dipole antennas. The feed network of the 9×9 array is designed using frequency-dependent input impedances to account for polarization isolation. The 9×9 array achieves a measured peak gain of 26.6 dBi and a total efficiency of 90% for LHCP and RHCP over the 26–41 GHz band (47%), with isolation below 40 dB between the two polarizations.

Author Contributions: Oludayo Sokunbi and Ahmed A. Kishk contributed equally to this work.

Conflicts of Interest: The authors declare no conflict of interest.

References

[1] B. Toh, R. Cahill, and V. Fusco, "Understanding and measuring circular polarization," *IEEE Trans. Educ.*, vol. 46, no. 3, pp. 313–318, Aug. 2003. [CrossRef]

[2] M. Rad, N. Nikkhah, B. Zakeri, and M. Yazdi, "Wideband Dielectric Resonator Antenna With Dual Circular Polarization," *IEEE Trans. Antennas Propag.*, vol. 70, no. 1, pp. 714–719, Jan. 2022. [CrossRef]

[3] S. Lu and S.-W. Qu, "Dual-Circularly Polarized Phased Array With Modified Cavity and Notched Patch," *IEEE Antennas Wireless Propag. Lett.*, vol. 23, no. 4, pp. 1266–1270, Apr. 2024. [CrossRef]

[4] Y.-H. Yang, B.-H. Sun, and J.-L. Guo, "A Low-Cost, Single-Layer, Dual Circularly Polarized Antenna for Millimeter-Wave Applications," *IEEE Antennas Wireless Propag. Lett.*, vol. 18, no. 4, pp. 651–655, Apr. 2019. [CrossRef]

[5] Y. Cheng and Y. Dong, "Dual Circularly Polarized Broadband Antenna Array for Millimeter-Wave Applications," *IEEE Antennas Wireless Propag. Lett.*, vol. 21, no. 12, pp. 2377–2381, Dec. 2022. [CrossRef]

[6] Y. Liu, Z. Yue, Y. Jia, Y. Xu, and Q. Xue, "Dual-Band Dual-Circularly Polarized Antenna Array With Printed Ridge Gap Waveguide," *IEEE Trans. Antennas Propag.*, vol. 69, no. 8, pp. 5118–5123, Aug. 2021. [CrossRef]

[7] Z. H. Jiang, T. Yue, and W. Hong, "Low-Profile and Wideband Dual-Circularly Polarized Reflect-Arrays Based on Rotated Metal-Backed Dual-Polarized Aperture-Coupled Patch Elements," *IEEE Trans. Antennas Propag.*, vol. 68, no. 3, pp. 2108–2117, Mar. 2020. [CrossRef]

[8] Z. Qi, Y. Zhu, and X. Li, "Compact Wideband Circularly Polarized Patch Antenna Array Using Self-Sequential Rotation Technology," *IEEE Antennas Wireless Propag. Lett.*, vol. 21, no. 4, pp. 700–704, Apr. 2022. [CrossRef]

[9] N. An and Y. Zhang, "Dual-Band Dual-Sense Circularly Polarized Antenna Utilizing a Radiating Slot Antenna as Feeding Structure," *IEEE Antennas Wireless Propag. Lett.*, vol. 23, no. 4, pp. 1321–1325, Apr. 2024. [CrossRef]

[10] M. A. Sofi, K. Saurav, and S. K. Koul, "Four-Port Orthogonal Circularly Polarized Dual-Band MIMO Antenna With Polarization and Spatial Diversity Using a Dual-Band Linear-to-Circular Polarization Converter," *IEEE Trans. Antennas Propag.*, vol. 70, no. 9, pp. 8554–8559, Sep. 2022. [CrossRef]

[11] P. Yang, R. Dang, and L. Li, "Dual-Linear-to-Circular Polarization Converter Based Polarization-Twisting Metasurface Antenna for Generating Dual Band Dual Circularly Polarized Radiation in Ku-Band," *IEEE Trans. Antennas Propag.*, vol. 70, no. 10, pp. 9877–9881, Oct. 2022. [CrossRef]

[12] R. Orr, G. Goussetis, and V. Fusco, "Design Method for Circularly Polarized Fabry–Perot Cavity Antennas," *IEEE Trans. Antennas Propag.*, vol. 62, no. 1, pp. 19–26, Jan. 2014. [CrossRef]

[13] P. Yang, R. Yang, and Y. Li, "Dual Circularly Polarized Split Beam Generation by a Metasurface Sandwich-Based Fabry–Pérot Resonator Antenna in Ku-Band," *IEEE Antennas Wireless Propag. Lett.*, vol. 20, no. 6, pp. 933–937, Jun. 2021. [CrossRef]

[14] Y. Yu, M. Sun, Z. Zhang, M. Guan, M. Wang, and A. Chen, "A Tunable Dual-Circularly Polarized Antenna With Broadband Triple-Branched Feed Structure," *IEEE Antennas Wireless Propag. Lett.*, vol. 21, no. 10, pp. 1965–1969, Oct. 2022. [CrossRef]

[15] H.-T. Hu, K. F. Chan, and C. H. Chan, "High-Gain Dual-Circular-Polarized Filtering Lens Antenna for Low-Cost 60 GHz Applications," *IEEE Antennas Wireless Propag. Lett.*, vol. 23, no. 2, pp. 828–832, Feb. 2024. [CrossRef]

[16] Z. H. Jiang, M. D. Gregory, and D. H. Werner, "Design and Experimental Investigation of a Compact Circularly Polarized Integrated Filtering Antenna for Wearable Biotelemetric Devices," *IEEE Trans. Biomed. Circuits Syst.*, vol. 10, no. 2, pp. 328–338, Apr. 2016. [CrossRef]

[17] A. K. Sahoo, R. D. Gupta, and M. S. Parihar, "Circularly polarised filtering dielectric resonator antenna for X-band applications," *IET Microw. Antennas Propag.*, vol. 12, no. 9, pp. 1514–1518, Jul. 2018. [CrossRef]

[18] Y. Dong, S. Gao, Q. Luo, L. Wen, C.-X. Mao, S.-W. Dong, X. Li, G. Wei, G. Wen, Y. Geng, and Z. Cheng, "Broadband Circularly Polarized Filtering Antennas," *IEEE Access*, vol. 6, pp. 76 302–76 312, 2018. [CrossRef]

[19] T. Li and X. Gong, "Vertical Integration of High-Q Filter With Circularly Polarized Patch Antenna With Enhanced Impedance-Axial Ratio Bandwidth," *IEEE Trans. Microw. Theory Techn.*, vol. 66, no. 6, pp. 3119–3128, Jun. 2018. [CrossRef]

[20] Z. H. Jiang and D. H. Werner, "A Compact, Wideband Circularly Polarized Co-designed Filtering Antenna and Its Application for Wearable Devices With Low SAR," *IEEE Trans. Antennas Propag.*, vol. 63, no. 9, pp. 3808–3818, Sep. 2015. [CrossRef]

[21] Q.-S. Wu, X. Zhang, and L. Zhu, "Co-Design of a Wideband Circularly Polarized Filtering Patch Antenna With Three Minima in Axial Ratio Response," *IEEE Trans. Antennas Propag.*, vol. 66, no. 10, pp. 5022–5030, Oct. 2018. [CrossRef]

[22] J.-F. Li, D.-L. Wu, G. Zhang, Y.-J. Wu, and C.-X. Mao, "A Left/Right-Handed Dual Circularly-Polarized Antenna With Duplexing and Filtering Performance," *IEEE Access*, vol. 7, pp. 35 431–35 437, 2019. [CrossRef]

[23] W. Wang, C. Chen, S. Wang, and W. Wu, "Circularly Polarized Patch Antenna With Filtering Performance Using Polarization Isolation and Dispersive Delay Line," *IEEE Antennas Wireless Propag. Lett.*, vol. 19, no. 8, pp. 1457–1461, Aug. 2020. [CrossRef]

[24] M.-C. Tang, D. Li, Y. Wang, K.-Z. Hu, and R. W. Ziolkowski, "Compact, Low-Profile, Linearly and Circularly Polarized Filtennas Enabled With Custom-Designed Feed-Probe Structures," *IEEE Trans. Antennas Propag.*, vol. 68, no. 7, pp. 5247–5256, Jul. 2020. [CrossRef]

[25] Q.-S. Wu, X. Zhang, L. Zhu, Z.-P. Zhong, J. Wang, K. Yu, G. Zhang, and C.-B. Guo, "Linearly and circularly polarized filtering patch antennas with enhanced gain selectivity on a single-layer substrate," *Int. J. RF Microw. Comput.-Aided Eng.*, vol. 32, no. 3, Mar. 2022. [CrossRef]

[26] G.-H. Sun and H. Wong, "Millimeter-Wave High-Gain Magneto-Electric Dipole Antenna Array With Pillbox Corporate Feed Network," *IEEE Trans. Antennas Propag.*, vol. 69, no. 9, pp. 5631–5639, Sep. 2021. [CrossRef]

[27] Q.-D. Cao, X.-X. Yang, F. Yu, and S. Gao, "High Scanning Rate Millimeter-Wave Circularly Polarized CTS Leaky Wave Antenna," *IEEE Trans. Antennas Propag.*, vol. 72, no. 7, pp. 6087–6092, Jul. 2024. [CrossRef]

[28] D. Li, L. Shi, J. Wang, Y. Liu, and Q. Chen, "High-Gain Wideband Dielectric Resonator Antenna Based on Semi-Cylindrical Grooved Structure," *IEEE Trans. Circuits Syst. II*, vol. 71, no. 3, pp. 1101–1105, Mar. 2024. [CrossRef]

[29] T. Ding, M. Wang, A. Kou, C.-Z. Han, and J. Xiao, "High-Gain Circularly Polarized Array Antenna Based on High-Order Mode ESIC for 5G Millimeter-Wave Application," *IEEE Antennas Wireless Propag. Lett.*, vol. 23, no. 10, pp. 3063–3067, Oct. 2024. [CrossRef]

[30] Q.-Y. Guo, X. Yi, R. C. Lv, W. He, C. F. Yang, G. Shu, Y. Tian, and H. Wong, "A High-Gain, Wideband, Circularly Polarized Antenna With Multibeam Radiation for Millimeter-Wave Applications," *IEEE Trans. Antennas Propag.*, vol. 72, no. 2, pp. 1373–1384, Feb. 2024. [CrossRef]

[31] O. Sokunbi, H. Attia, A. Hamza, A. Shamim, Y. Yu, and A. A. Kishk, "New Self-Isolated Wideband MIMO Antenna System for 5G mm-Wave Applications Using Slot Characteristics," *IEEE Open J. Antennas Propag.*, vol. 4, pp. 81–90, 2023. [CrossRef]

[32] Q. Li, S. Liao, Y. Yang, Z. Liang, and S. Xiao, "Wideband 5G Millimeter-Wave MIMO Magnetoelectric Dipole Antenna Integrated With Partially Reflective Surfaces," *IEEE Trans. Antennas Propag.*, vol. 72, no. 1, pp. 445–453, Jan. 2024. [CrossRef]

[33] C. Zhu, G. Xu, A. Ren, W. Wang, Z. Huang, and X. Wu, "A Compact Dual-Band Dual-Circularly Polarized SIW Cavity-Backed Antenna Array for Millimeter-Wave Applications," *IEEE Antennas Wireless Propag. Lett.*, vol. 21, no. 8, pp. 1572–1576, Aug. 2022. [CrossRef]

[34] E. Rajo-Iglesias, M. Ferrando-Rocher, and A. U. Zaman, "Gap Waveguide Technology for Millimeter-Wave Antenna Systems," *IEEE Commun. Mag.*, vol. 56, no. 7, pp. 14–20, Jul. 2018. [CrossRef]

[35] A. A. Kishk and A. T. Hassan, "Design of Large Finite Array Antennas and its Feeding Network," in *2019 IEEE Int. Conf. on Comput. Electromagn. (ICCEM)*, Shanghai, China, 2019, pp. 1–3. [CrossRef]

[36] Y. Li, L. Ge, J. Wang, B. Ai, M. Chen, Z. Zhang, and Z. Li, "A Ka -Band 3-D-Printed Wideband Stepped Waveguide-Fed Magnetoelectric Dipole Antenna Array," *IEEE Trans. Antennas Propag.*, vol. 68, no. 4, pp. 2724–2735, Apr. 2020. [CrossRef]

[37] Y. Wu, T. Tomura, J. Hirokawa, and M. Zhang, "A Wideband Full-Metal Sidewall-Loaded Magnetoelectric Dipole Array Based on Combined Ridge and Groove Gap Waveguides in the Q-Band," *IEEE Trans. Antennas Propag.*, vol. 71, no. 7, pp. 6156–6161, Jul. 2023. [CrossRef]

[38] K. M. Luk, S. F. Zhou, Y. J. Li, F. Wu, K. B. Ng, C. H. Chan, and S. W. Pang, "A microfabricated low-profile wideband antenna array for terahertz communications," *Sci. Rep.*, vol. 7, no. 1, 2017, Art. no. 1268. [CrossRef]

[39] X. Li, J. Xiao, Z. Qi, and H. Zhu, "Broadband and High-Gain SIW-Fed Antenna Array for 5G Applications," *IEEE Access*, vol. 6, pp. 56 282–56 289, 2018. [CrossRef]

[40] P.-S. Kildal, E. Alfonso, A. Valero-Nogueira, and E. Rajo-Iglesias, "Local Metamaterial-Based Waveguides in Gaps Between Parallel Metal Plates," *IEEE Antennas Wireless Propag. Lett.*, vol. 8, pp. 84–87, 2009. [CrossRef]

[41] O. Sokunbi and A. Kishk, "Dual Polarized Planar Array of Metallic Magnetoelectric Dipoles," in *2025 19th European Conf. on Antennas and Propagation (EuCAP)*, Stockholm, Sweden, 2025, pp. 1–4. [CrossRef]

[42] Y. Zhao and K.-M. Luk, "Dual Circular-Polarized SIW-Fed High-Gain Scalable Antenna Array for 60 GHz Applications," *IEEE Trans. Antennas Propag.*, vol. 66, no. 3, pp. 1288–1298, Mar. 2018. [CrossRef]

[43] B. Feng, Y. Tu, J. Chen, K. L. Chung, and S. Sun, "High-performance dual circularly-polarized antenna arrays using 3D printing for 5G millimetre-wave communications," *AEÜ - Int. J. Electron. Commun.*, vol. 130, Feb. 2021, Art. no. 153569. [CrossRef]

[44] J. Wu, Y. J. Cheng, H. B. Wang, Y. C. Zhong, D. Ma, and Y. Fan, "A Wideband Dual Circularly Polarized Full-Corporate Waveguide Array Antenna Fed by Triple-Resonant Cavities," *IEEE Trans. Antennas Propag.*, vol. 65, no. 4, pp. 2135–2139, Apr. 2017. [CrossRef]

https://doi.org/10.64897/ieet.2025v1i1.001